# Transparent Glasses and Ceramics

# MESOMECHANICAL CONSTITUTIVE RELATIONS FOR GLASS AND CERAMIC ARMOR

D. R. Curran, D. A. Shockey, and J. W. Simons
SRI International
Menlo Park, CA 94025

## ABSTRACT

A major challenge in achieving a physics-based computational capability for designing glass and ceramic armor is a damage evolution and fragment flow model that is usable in continuum codes. We describe a model that uses microfailure and fragment flow constitutive data, show how the model links to continuum models, and compare computational results with glass penetration tests.

## BACKGROUND AND PROGRAM GOALS

Improved mesomechanical constitutive relations for glass targets undergoing microscopic damage are needed for efficient design of transparent armor. The role of the mesomechanical models is to relate material failure on the microscopic level to continuum behavior, and to give guidance to continuum models that are used in hydrocodes.

Penetration of thick targets of both ductile and brittle materials occurs by the formation of a region of yielded, flowing material at the penetrator–target interface. The flow of this material allows penetration to occur. For brittle materials like glass and ceramics, the yielded material is observed to consist of fine fragments in a thin region called the Mescall zone (MZ)[1].

Our goal is to construct a mesomodel that describes the microdamage evolution, i.e. the nucleation, growth, and coalescence of microcracks to form the MZ, and subsequent granular flow of the comminuted material out of the path of the advancing penetrator. Our mesomodel is empirical, and is based on observations and data from experiments designed to measure microdamage evolution and fragment flow.

In this paper we describe a proposed initial framework for a mesomodel, incorporate available data, discuss preliminary correlations of predictions with observations, and discuss future proposed experiments.

## MESOMECHANICAL APPROACH

Empirically-based mesomechaoical constitutive relations have been successfully developed during the past several decades to relate material failure in metals and composites to the underlying microscopic processes, thereby helping to select appropriate continuum models and resolve apparent paradoxes[2-4]. The key to this approach has been the development of experiments for determination of "nucleation and growth to fragmentation" (NAG/FRAG) laws in a relevant volume element (RVE) for the evolution of size distributions of microscopic voids and cracks and their coalescence to form fragments, as well as the subsequent motion of these fragments.

NAG/FRAG experiments are designed to measure key properties. As summarized in the 2004 book by Kanel, Razorenov, and Fortov[5], glass presents several challenges, as follows.

- Flaw sites: Whereas most brittle materials contain internal flaws that can serve as microcrack nucleation sites, high quality glass has primarily only surface flaws. This means that in uniaxial strain plate impact experiments, for example, the microdamage should be localized in a region adjacent to the impact surface.
- HEL: Glasses do not exhibit a distinct Hugoniot elastic limit in plate impact experiments, partly because of a convex downward curvature of the Hugoniot at low pressures.

Molecular structure: At high pressures, brittle glasses become ductile. The molecular structure of glass allows densification without cracking at pressures exceeding 7-10 GPa. At such pressures, evidence of

yield may vanish, and the response may be difficult to distinguish between elastic and hydrostatic.

Prior experiments have emphasized instrumented long and short rod penetration tests ranging from near the dwell transition to steady-state penetration. The measurements include x-ray or optical "snapshots" of the position of the macrocrack front, MZ front, and penetrator tail position[4,7]. However, until recently, experiments specifically designed to yield NAG/FRAG relations for the evolution of microscopic damage were lacking. In the present paper we focus on three types of experiments that can potentially provide such information:

1. Plate impact (uniaxial strain) experiments. These experiments simulate the loading conditions on-axis under the penetrator nose during the impact shock response.
2. Partial penetration of non-eroding rods. These experiments reproduce the loading conditions near the nose of elastic penetrators at penetration rates of several hundred m/s.
3. Quasistatic material property tests, including compression-torsion tests of powders. These experiments provide basic properties of the MZ material.

To guide planning and interpretation of the above experiments, we start with a conceptual mesomodel (CMM), which will serve as an initial framework to be modified as we obtain more microdamage evolution data.

## CONCEPTUAL MESOMECHANICAL MODEL

The CMM is based on modifications of the FRAGBED2 (FB2) mesomodel of non-elastic flow in brittle materials[8]. The non-elastic flow is assumed to be totally due to elastic fragments sliding frictionally on inter-fragment interfaces, and is treated by analogy to multi-plane plasticity models based on atomic dislocation dynamics, i.e. we focus on the movement of lines of holes between the fragments, called macrodislocations (MDs), on a finite number of slip planes. The flow is inherently rate-dependent because of finite crack nucleation and growth rates and fragment inertia. Linear Elastic Fracture Mechanics (LEFM) is assumed to govern the microcrack nucleation, and the "fracture toughness" is a property that represents the material's brittleness.

Micrographs of fragmented ceramics suggest that the fragmented bed is initially a jumbled array of different-sized fragments in which flow is inhibited because the fragments block each other, and the associated MDs are "pinned". The "yield" condition in the CMM is thus an "unpinning" condition. Figure 1 is a schematic of this situation, which also illustrates the expected importance of confining boundaries.

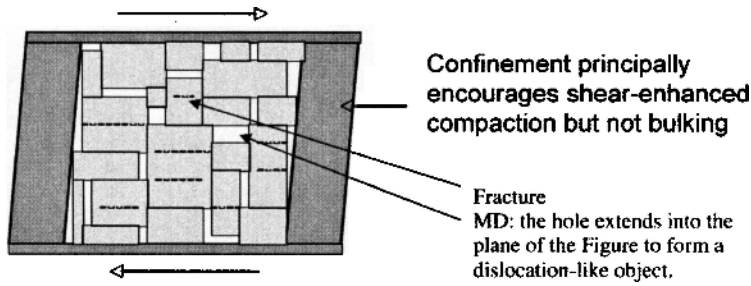


Figure 1. Schematic picture of conceptual mesomodel.

The proposed unpinning criterion is based on a simplification of the FB2 comminution model. We assume that an applied remote "driving stress" state (τ, P) is sufficient to fracture fragments of size $B_{ic}$ or greater, given by

$$\eta B_{II} = \pi K_{Ic}^2/4(m_1\tau^2 + m_2P^2) \quad (1)$$

where $\tau$ is the maximum shear stress, P is the pressure, $B_{II}$ is a critical fragment size, $\eta B_{II}$ is the corresponding critical flaw size, $K_{Ic}$ is the plane strain fracture toughness, and the m's allow local stress enhancement over the remote stresses. Figure 1 shows that we idealize the fragment cross-sections as squares. An equivalent circle with the same area would thus have a radius $R = B/\pi^{1/2} = 0.56B$.

Eq (1) is clearly an oversimplified relation to be improved as more data are obtained. For example, the dynamic initiation or arrest toughness and/or a combination of Mode I and Mode II toughnesses would be more appropriate than $K_{Ic}$, which is used here as a simple measure of brittleness, and to show trends. We expect that a more detailed model, such as that of Simons et al[5] for concrete and marble, may eventually be needed.

As the applied stresses increase, comminution breaks down the larger fragments until either sufficient unpinning has occurred to allow flow of the remaining fragments, or comminution ceases because the flaw sizes are subcritical.

Specifically, we fit our data to an initial Poisson fragment size distribution

$$N_2(B) = N\exp(-B/B_0) \quad (2)$$

where $N_2(B)$ is the number of fragments per unit area of a cross section with size greater than B, N is the total number of fragments per unit area in a cross section, and $B_0$ is the initial average size of the fragments[4]. The fragment density function is

$$dN/dB = (N/B_0)\exp(-B/B_0) \quad (3)$$

We assume that the initial distribution has an upper cutoff, a largest fragment, $B_{max}$. We also assume that the initial hole (MD) size distribution mirrors the fragment size distribution, with the larger holes being associated with the larger fragments, and the average hole size is equal to the average fragment size. Integrating the hole area $bB^2$ with a density function like Eq(3) from B = 0 to $B_{max}$ gives the total initial porosity

$$\phi_T = N_H bB_0^2[2 - f(x)] \quad (4a)$$

where $N_H$ is the total number of holes per unit area of a cross section, b is the fraction of B that specifies the width of the hole, i.e. bB is the macroscopic Burger's vector, and

$$f(x) = (x^2+2x+2)\exp(-x) \quad (4b)$$

where $x = B_{max}/B_0$.

For a given B, say $B_1$, the mobile porosity is the total porosity minus the integral from 0 to $B_1$, and the ratio of mobile to total porosity is

$$\phi_M/\phi_T = |f(x_1) - f(x_2)|/|2 - f(x_2)| \quad (5)$$

where $x_1 = B_1/B_0$, and $x_2 = B_{max}/B_0$.

For example, Eq(5) shows that when $B_1 = B_0$, and $B_{max} = 2\ B_0$, $\phi_M/\phi_T = 0.75$. That is, when the largest fragment in the distribution has been reduced to $B_0$, 75% of the original fragments and associated MDs have been unpinned.

For such flow to be possible, the material must contain pores (the MDs). Under the high confinement provided by the impact interface of a uniaxial strain plate impact, or on-axis at the nose of a rod impact, the MDs will tend to be driven into the confining boundary, resulting in compaction (the fragments can move into the RVE, but not out). If the confinement is maintained, the subsequent response must be elastic. This postulated behavior is shown schematically in Figure 2.

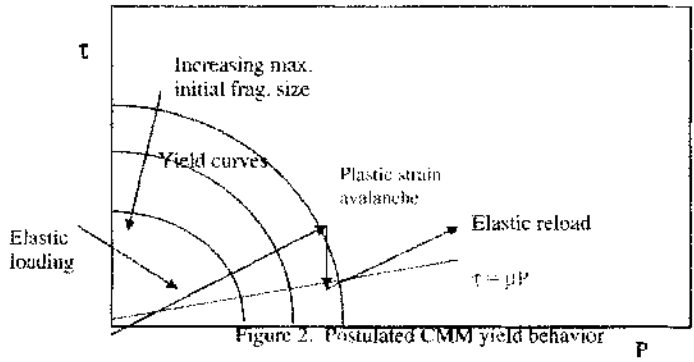


Figure 2. Postulated CMM yield behavior

The mesomodel must also describe the process by which tensile cracks and MDs (voids) are produced in originally void-free glass under compression and shear. "Wing cracks" are a candidate for causing brittle failure and dilatancy under compression and shear (see Figure 3). In general, a weak shear surface flaw can either propagate as a Mode II shear crack, or turn out of the crack plane and propagate as a wing ("splitting") crack. In the latter case, voids (MDs) are produced in the target, causing dilatancy. The extensive literature on this subject is reviewed in the 2004 book by Kanel, Razorenov, and Fortov[5]. Wing cracks were observed in glass plates under compression in 1963 by Brace and Bombolakis[10]. Subsequent work by Nemat-Nasser and Horii[11], Horii and Nemat-Nasser[12], Moss and Gupta[13], and Nemat-Nasser and Obata[14], among others, described expected behavior under different stress states. Kalthoff[15] performed experiments with an edge impact technique on a number of ductile and brittle materials, and found that the mode chosen depended on whether there was a mechanism for shear softening (e.g. adiabatic heating) sufficient to stabilize a propagating shear crack.

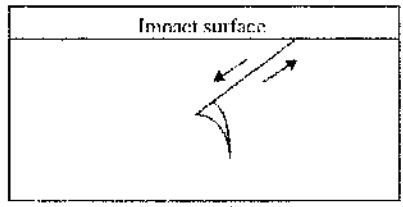


Figure 3. Wing crack

Thus, wing cracks appear to be a possible source for driving voids (MDs) into previously non-porous glass in plate impact tests. However, the brittle-ductile transition discussed above may suppress their formation, in which case we would expect a non-porous layer of damage at the impactor-target interface. To resolve this and other issues, we need more data.

## SUPPORTING EXPERIMENTS

### Uniaxial strain plate impact response:

We begin by examining the response of Soda-Lime Glass (SLG) samples loaded by uniaxial strain impacts in experiments reported by Sinha and Gupta[16], and Alexander et al[17]. We assume that

cracks (wing cracks or shear cracks), originate from a size distribution of flaws of size $\delta$ on the impacted surface. We also assume that the distribution is of the form of Eq(2). To relate the flaw size to the fragment size B, we draw on the "crack range" concept of the BFRACT model for tensile cracks[4], which defines a parameter $M = B/\delta$. For very brittle materials, M can be between 10 and 20. The FB2 comminution model assumes that each fragment contains a flaw of size $\delta = \eta B$. Thus, $M = 1/\eta$.

For each active slip plane, Eq (1), with $\delta$ set equal to the minimum flaw size, describes the Fig. 2 yield function in $\tau - P$ space. When an elastic load path crosses the surface, the model produces a burst of non-elastic strain as the porosity is driven into the impactor surface. The shear stress drops at constant pressure to the "failed" curve $\tau = \mu P$.

To describe the non-elastic flow of the "yielded" material in a manner that ensures stability and uniqueness, an analysis due to Whitham[14,19] is applied, and a "stress-relaxing solid" relation is used to describe the total strain rate on a slip plane as the sum of the elastic strain rate and the non-elastic strain rate:

$$\partial\varepsilon/\partial t = (1/2G)\,\partial\tau/\partial t + \partial\varepsilon^{ie}/\partial t \qquad (6a)$$

where the non-elastic strain rate is given by

$$\partial\varepsilon^{ie}/\partial t = [\phi/2(2b)^{1/2}B]\{(\tau-\mu P)/\rho\}^{1/2}\,H(\tau-\mu P) \qquad (6b)$$

and where G is the shear modulus, H is the Heaviside function, $\tau$ is the maximum shear stress ($= \sigma_{xx}/2$), $\mu$ is the intergranular friction coefficient, $\phi$ is the mobile (unpinned) porosity associated with the MDs, B is the average hole (MD) height (equal to the average fragment size), and b is a dimensionless parameter that characterizes the average MD width. The quantity $[\phi/(b)^{1/2}B]$ can be considered a meso-parameter that specifies, for a given stress state on a given slip plane, both the porosity carried by a MD and the MD speed. It has significant leverage on the predicted behavior, and we will vary it in a parameter study.

In Table 1, we list measured and assumed material properties for the Soda-Lime Glass (SLG), and compare them with those for $B_4C$, a ceramic for which a clear two-wave response has been measured[20]. The glass and $B_4C$ data warrant continued study, since both sets of experiments were well-instrumented, and give an opportunity to study the effects of different microstructures, fracture toughnesses, and moduli.

Table 1. Properties for SLG and B4C

| PROPERTY | SLG | B4C |
|---|---|---|
| Density (g/cc) | 2.5 | 2.51 |
| $C_L$ (km/s) | 5.761 | 13.7 |
| $C_S$ (km/s) | 3.437 | 8.7 |
| $C_{bulk}$ (km/s) | 4.176 | 9.3 |
| $\nu$ (Poissons ratio) | 0.224 | 0.162 |
| G | 12 MPa* (29.5 GPa) | 190 GPa |
| K | 17 MPa* (43 Gpa) | 218 GPa |
| E | 29 MPa* (73 GPa) | |
| $K_{Ic}$ (MPa-$m^{1/2}$) | 0.9 | 4 |
| HEL (GPa) | 3.5 – 7 | 16.15 |
| Flaw locations | Surface | Surface and internal; grain boundaries, inclusions, etc. |
| Assumed meso properties, $\mu$, $\eta$, $B_1$, $B_0$, $B_{min}$, $\phi/b^{1/2}B_0$ | 0.3, 0.1, 1μm, 50 μm, 100μm, 10 - 100 $cm^{-1}$ | |

* The reported[17] ambient pressure elastic moduli measured by ultrasound are inconsistent with the measured wave speeds, and have been corrected. The corrected values are given in the parenthesis.

We do not have measurements of the surface flaw distributions in the glass, but we will do an example analysis assuming the mesomechanical properties listed in Table 1, including setting $B_1$ = 1 μm, $B_0$ = 50 μm, and $B_{max}$ = 100μm. We next apply the simplified flow model of Eq (6b).
To convert the τ relations to those for the longitudinal stress, S, we use the uniaxial strain conditions:

$$\tau = [3(1-2\nu)/2(1+\nu)] \quad P = P/\psi, \text{ where } \psi = [2(1+\nu)/(3(1-2\nu)], \text{ and } S = [2(1-\nu)/(1-2\nu]\tau \tag{7}$$

Operating on Eq (6a) with $\partial/\partial t$, combining with the equations for conservation of mass and momentum, and using the above uniaxial strain relations connecting S and τ via Poisson's ratio ν, leads to

$$\partial^2 S/\partial t^2 - C^2\partial^2 S/\partial h^2 + \lambda(\partial S/\partial t) = 0 \tag{8}$$

where h is the Lagrangian distance into the target, C is the longitudinal wave speed,

$$\lambda = (1/T) = [(1-2\nu)/2(1-\nu)]^{1/2}\,[1-\mu\psi]^{1/2}\,[0.18\phi/b^{1/2}B]\rho^{1/2}C^2S^{1/2} \tag{9}$$
$$\text{and } \psi = [2(1+\nu)/(3(1-2\nu)].$$

Using the glass values of Table 1 yields values of T = ranging from 50 to 500 ns, depending on the choice of $\phi/b^{1/2}B_0$.

Eqs (8) and (9) fulfill a stability criterion due to Whitham[18,19]: If $\lambda \neq 0$, the solution to Eq(8) for S(h,t) is well-posed and stable (dissipative). The result is a decaying elastic wave followed by a diffusive failure wave. In the linear approximation, S is given by

$$S \approx S_0(t-h/C)\exp[-\lambda h/2C] \tag{10}$$

where $S_0$ is the impact stress. Thus, the width of the MZ is approximately 2CT. λ in Eq(9) is not a constant, but depends on the stress to the -1/2 power, thereby violating the linear assumption. However, the "viscous" overshoot from the HEL is small, so we will roughly approximate the response by setting S equal to the HEL value.

We now focus on specific experiments with SLG glass performed by Simha and Gupta and Alexander et al, in which SLG impactors on SLG targets generated elastic impact stresses of 4 to 10 GPa at the impact surface. Both measured loading times to 4 GPa of about 0.2μs. For impact stresses of 4 to 6 GPa, Simha and Gupta measured a two-wave structure. For example, at 4.6 GPa, they measured a slightly rounded longitudinal stress plateau at 4 GPa, followed after about 2 μs by a second rise to 4.6 GPa. This can be combined with their lateral stress history record to show a strength, τ, that jumps to a plateau of about 1.5 GPa, but after about 0.5 μs, drops to about 1 GPa, only to ramp up again at about 2.5 μs to a new plateau of about 1.5 GPa at about 3 μs. This observed two-wave structure was interpreted by Simha and Gupta as a time-dependent loss of strength followed by a partial regaining of that strength, consistent with the CMM picture. In contrast, Alexander et al did not record a two-wave structure.

Simha and Gupta developed an ad hoc continuum strength model that correlated well with the above experiments, has similar features as the CMM model, and can therefore serve as a test of the CMM model's validity.

That is, to compare the CMM predicted trends with the above data, we set $m_1 = m_2 = 1$, and choose the parameters in Table 1 to enforce a value of 4 GPa for the HEL. The values in Table 1 for SLG give a uniaxial strain loading path of $\tau = 0.68P$, and Eq (1) gives a yield circle with a radius = 2.5

GPa, corresponding to S (HEL) = 4 GPa, as desired. The CMM model calculates a diffusion front pseudovelocity obtained by analogy to heat flow calculations[3], where calculations of heat flow from a hot slab, maintained at constant temperature, suddenly placed in contact with a cold material, showed that the pseudovelocity of propagation of one-fourth the hot slab temperature, was 3k/h, where k is the diffusivity. Taking the diffusivity to be equal to $C^2$ T, and setting the pseudovelocity equal to h(diffusion)/t yields

$$h(\text{diffusion}) = 1.7C(Tt)^{1/2} \tag{11}$$

So far, the discussion has concerned individual slip planes, but a further consequence of the postulated "unpinning yield condition" is that many slip planes would become active simultaneously. In Figure 1, for example, the vertical slip planes would also start to slide. The fragment cross sections, schematically shown as squares, would become "rounder", and the material would become more like a liquid. The effective coefficient of friction $\mu$ might decrease as the particles begin to roll. But if the confinement is maintained, once the MDs have flowed into the confining penetrator interface to compact the material, the subsequent reloading from the relaxed state S ($\tau = \mu P$) of 1.74 GPa (for $\mu$ = 0.3) would be that of an elastic liquid, and the appropriate wave speed would be the bulk wave speed.

Since the CMM model has many adjustable parameters, a wide variety of responses can be predicted. We performed a preliminary parameter study by varying the value of $\phi/b^{1/2}B_0$ over the range shown in Table 1. Figure 4 shows the two extremes (T = 50 ns and T = 500 ns) for the Simha and Gupta experiment which produced an impact stress of 4.6 GPa. The best overall correlation is obtained with the large value of T (500 ns), which forced the diffusing failure wave to travel at almost the elastic wave speed. The slower bulk wave speed for the elastic liquid delayed the arrival of the reloading wave to about 1.6 μs, in rough agreement with the Simra and Gupta results for the longitudinal stress. However, the observed regaining of strength is not predicted by the CMM (although it is possible to imagine that the fine particles compact and "freeze" to become an effective solid again).

By choosing the small value of T (50 ns), we can delay the reloading pulse to agree with the second wave arrival time recorded by Simha and Gupta. However, Figure 4 shows that the delay simply reduces the first wave to low amplitude, resulting in a poor correlation.

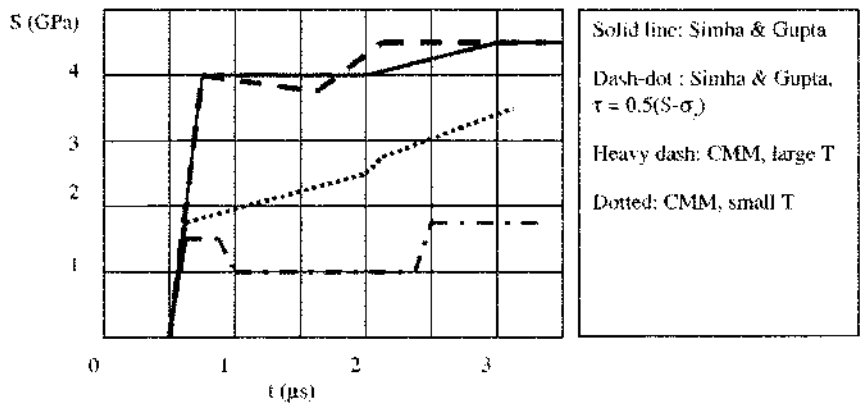


Figure 4. Comparison of CMM model trends with simplified Simha & Gupta data. Measurement is 3 mm from impact surface.

At higher impact stresses, the data suggest that the glass becomes ductile, and/or undergoes densification or a phase change, and no longer behaves like a collection of elastic fragments. Since our model predicts that the material will recompact at the impactor interface, and reload elastically, we expect that both reshocking and unloading should occur elastically, as diagrammed schematically in Figure 2. Elastic unloading was, in fact, inferred by Alexander et al[6].

In summary, there are enough adjustable parameters in the CMM model to allow rough trend correlations with the plate impact data to be obtained, but we need additional damage evolution data to further constrain our model parameters. A proposed "soft recovery" plate impact experiment will be described later.

Partial penetration experiments provide valuable data under other loading conditions, and are discussed next.

Partial penetration of non-eroding rods:

As described in a companion paper in the present conference[2], we have performed experiments in which hard steel hemispherical-nosed rods were fired into thick, confined soda lime and borosilicate glass targets at impact velocities ranging from 300 to 600 m/s. The 6.35 mm diameter x 31.8 mm long rods remained elastic, and arrested after partial penetration. The recovered targets showed a MZ region around the penetrator that consisted of pulverized material with a fairly sharp boundary. The MZ thickness at the nose at arrest in all cases was less than 2 mm. The diameter of the tunnel ranged from about twice the rod diameter at 300 m/s impact velocity to about 4 times the rod diameter at 600 m/s impact velocity.

The membrane stresses nucleate finely-spaced cone cracks which are driven into the target from the rod periphery as the rod advances, and intersect with less finely-spaced lateral cracks to form a fragmented bed ranging from mm-sized fragments some distance ahead of the arrested penetrator to sub mm-sized fragments close to the boundary with the MZ, within which the fragment sizes were less than 50 microns. The cone cracks open to relieve the stress and produce porosity (MDs). Thus, similar to the potential role played by wing cracks in the plate impact case, a mechanism exists to produce both fragments and porosity (MDs) in a region ahead of an oncoming interface with the impenetrable penetrator or flyer plate.

The CMM model then suggests the following penetration scenario. When the axial compressive stress at a given location (RVE) ahead of the penetrator reaches the critical value for the largest fragments in the RVE (Fig. 2), those fragments and MDs are unpinned, and non-elastic flow begins. This flow initially consists of "channels" of small fragments carrying larger "colonies" into the tunnel[3]. The higher pressures near the penetrator nose cause comminution and production of micron-sized particles similar to those in the plate impact case. The porosity is absorbed by the penetrator nose, resulting in a compacted MZ. Then flow of the MZ material begins from the penetrator periphery, allowing the penetrator to advance. However, the flowing powder also interacts with the penetrator material to abrade it, and the temperatures are high enough to melt some of the glass, as observed[2].

Preliminary measurements[3] of the fragment size distribution in the MZ close to the penetrator's nose roughly fit a Poisson distribution with $B_o$ in Eq (2) equal to about 50 microns inside the MZ boundary and 60 microns outside the boundary. If we now assume that $\eta$ is 0.1 and $B_o$ = 50 microns, Eq(1) gives a critical driving stress of 0.3 GPa for the outer boundary of the MZ. This appears to correlate well with supporting hydrocode calculations at an impact velocity of 400 m/s[2]. Furthermore, the hydrocode calculations give a driving stress near the interface of about 2.5 to 3 GPa, which Eq(1) predicts will produce fragments a little less than 1 micron in size, which also correlates reasonably well with micrographs of the fragments adhered to the penetrator nose surface[2]. In this scenario, the main role of the larger fragments in the MZ, as well as the fragments outside the MZ, is to provide the porosity that initially allows flow.

Thus, the CMM correlations are perhaps encouraging, but we again need more microdamage evolution data, as discussed next.

## FUTURE TEST PROGRAM

Partial penetration tests:

The partial penetration tests fulfill the basic requirements for measuring microdamage evolution: variable load amplitudes and durations, soft-recovered specimens allowing microscopic examination of the fractured material, and recovered tunnel material for property testing. A prototype test program is described in a companion paper in this conference[2].

Quasistatic property tests:

Tests are needed to obtain basic material properties, especially for the pulverized material, for input to both continuum and mesomechanical models. Pressure–shear measurements on pulverized material recovered from the partial penetration tests are underway[2]. Those tests include microstructural observations of the material before and after granular flow. We plan similar observations of damaged material from confined pressure tests being performed at SwRI. Since interaction of the pulverized material debris with the penetrator nose and sides seemed important in the partial penetration tests, we plan to also examine the material that adheres to the shear surfaces in the SwRI specimens. We will compare the evolution of fragment size and shape for the two cases.

Soft-recovered plate impact tests:

To help interpret prior plate impact data, we need tests that allow us to measure the evolution of the microdamage. In prior work on brittle tensile fracture and fragmentation in Armco iron, for example, we were able to produce different damage levels in target "pucks", and thereafter perform iterative calculations with NAG/TRAG models until we could correlate with the measured damage distributions[4]. To follow the same procedure for compression-shear loads, we need a scheme to soft-recover the target specimens for subsequent microscopic examination. A possible design is sketched in Figure 5, which shows the following features based on our earlier work[3,4]:

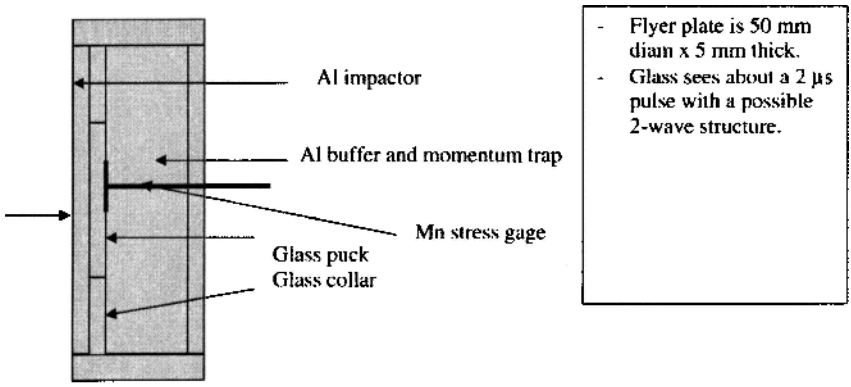


Figure 5. Plate impact test design

- The samples are intact or pre-fractured cylindrical glass plates ("pucks").
- Impactor and confinement materials are impedance-matching aluminum alloys.
- The sample plate is surrounded by a glass collar whose purpose is to eliminate converging unloading waves, and maintain uniaxial strain in the sample for the duration of the load pulse.
- Impact velocities and transmitted stress histories are measured.
- Increasing impact velocity levels produce increasing degrees of damage.
- A standard "rag cage" is used for soft-recovery of the target package.
- The glass sample is characterized pre and post-test for fragment size, pore size, and fragment geometry distributions.

## CONCLUSIONS

Our conceptual mesomodel (CMM) shows some promise, but needs more microdamage evolution data to improve it. As discussed above, we expect that Eq(1) will be replaced by an expression that contains static and dynamic Mode I and Mode II toughnesses and other refinements, and sophisticated crack growth and coalescence models are available for correlating better with microdamage evolution data. Some key questions are:

- How is dilatancy introduced in impacted glass targets free of internal flaws? Are wing cracks the actual mechanism? The proposed experiments of Figure 5 should help us answer that and other questions.
- What governs the sudden reduction of fragment sizes inside the MZ? The picture of "strain burst"–induced compaction followed by elastic reloading under confinement and compaction will no doubt be modified by data from the proposed additional partial penetration tests and plate impact tests.
- What are the flow properties of the material in the MZ? Data from the planned quasistatic property tests will be valuable in this area.

In general, the forthcoming detailed microscopic damage evolution data should help us replace uncertain elements of our conceptual mesomodel with empirically-determined relations.

## ACKNOWLEDGMENTS

This work was funded by the U.S. Tank Automotive Command under subcontract to Southwest Research Institute. The authors are grateful to D. W. Templeton of TACOM and C. E. Anderson, Jr. and his team for their interest and support.

## REFERENCES

[1]D. A. Shockey, A. H. Marchand, S. R. Skaggs, G. E. Cort, M. W. Burkett, and R. Parker, "Failure Phenomenology of Confined Ceramic Targets and Impacting Rods", Int. J. Impact Engr, Vol 9 (3), pp. 263-275, (2000).

[2]D. A. Shockey, D. Bergmannshoff, D. R. Curran, and J. W. Simons, "Failure Physics of Glass during Ballistic Penetration", Proceedings of the 32nd International Conference & Exposition on Advanced Ceramics & Composites (ICACC), held at Daytona Beach, FLA, Jan. 27 – Feb. 1, 2008.

[3]D. A. Shockey, "Rosetta Stone Experiments, and a Mesomechanical Approach to High Strain-rate Deformation and Fracture", SEM William M. Murray Lecture, Experimental Mechanics, DOI 10.1007/s11340-006-9030-8, (June 7, 2006).

[4]D. R. Curran, L. Seaman and D. A. Shockey, "Dynamic Failure of Solids", Physics Reports, Vol. 47, Nos. 5 & 6, March 1987.

[5]G. I. Kanel, S. V. Razorenov, and V. E. Fortov, Shock-Wave Phenomena and the Properties of Condensed Matter, Springer-Verlag, New York (2004).

[6]Th. Behner, Ch. E. Anderson Jr., D. L. Orphal, M. Wickert, V. Hohler, and D. W. Templeton, "Failure and Penetration Response of Borosilicate Glass during Short Rod Impact", Proc. 23rd Int. Symp. Ballistics, **2**, pp 1251-1258, Graficas Couche, Madrid, Spain, (2007).
[7]C. E. Anderson Jr., T. Behner, T. J. Holmquist, M. Wickert, V. Hohler, and D. W. Templeton, "Interface defeat of long rods impacting borosilicate glass", Proc. 23rd Int. Symp. Ballistics, **2**, pp 1049-1056, Graficas Couche, Madrid, Spain, (2007).
[8]D. R. Curran, "Comparison of Mesomechanical and Continuum Granular Flow Models for Ceramics", Proceedings of the APS SCCM Topical Conference, 31 July-6 August 2005, Baltimore Md.
[9]J. W. Simons, T. H. Antoun, and D. R. Curran, "A Finite Element Model for Analyzing the Dynamic Cracking Response of Concrete", Presented at the 8th International Symposium on Interaction of the Effects of Munitions with Structures, McClean, Virginia, (April 22-25, 1997).
[10]W. F. Brace and E. G. Bombolakis, "A Note on Brittle Crack Growth in Compression", J. Geophys. Res. **68**, pp. 3709-3713, (1963).
[11]S. Nemat-Nasser and H. Horii, "Compression-induced Nonplanar Crack Extension with Application to Splitting, Exfolation, and Rockburst", J. Geophys. Res. **87(B8)**, pp. 6805-6821, (1982).
[12]H. Horii and S. Nemat-Nasser, "Compression-induced Macrocrack Crack Growth in Brittle Solids: Axial Splitting and Shear Failure", J. Geophys. Res. **90(B4)**, pp. 3105-3125, (1985).
[13]W. C. Moss and Y. Gupta, "A Constitutive Model Describing Dilatancy and Cracking in Brittle Materials", J. Geophys. Res. **87(B4)**, pp. 2985-2998, (1982).
[14]S. Nemat-Nasser and M. Obata, "A Microcrack Model of Dilatancy in Brittle Materials", Trans. ASME: J. Appl. Mech. **55(110)**, pp. 24-35, (1988).
[15]J.F. Kalthoff, "Modes of dynamic shear failure in solids", Int. J. Fracture **101**, pp. 1-31, (2000).
[16]C. H. M. Simha and Y. M. Gupta, "Time Dependent Inelastic Deformation of Shocked Soda-lime Glass", J. Appl. Physics, Vol. 96, No. 4, pp 1880-1890, (15 August, 2004)
[17]C. S. Alexander, L. C. Chhabildas, and D. W. Templeton, "The Hugoniot Elastic Limit of Soda-lime Glass", in Shock Compression of Condensed Matter – 2007 (M. Elert, M. D. Furnish, R. Chau, N. Holmes and J. Nguyen eds., AIP Press, pp 733-738 (2007).
[18]G. B. Whitham, " Some Comments on Wave Propagation and Shock Wave Structure with Application to Magnetohydrodynamics", Comm. Pure and Applied Mathematics, Vol. XII , 113-158, (1959)].
[19]G. B. Whitham, Linear and Nonlinear Waves, John Wiley & Sons, 1974.
[20]T. J. Holmquist and G. R. Johnson, "Characterization and Evaluation of Boron Carbide for 1D Plate Impact", Tech. Report: SwRI report 18.10174/03, Contract F42620-00-D-0037-DR02, (July 2006).
[21] C. E. Anderson, personal communication.